High energy asymmetric supercapacitor based on nickel cobalt oxide (NiCo$_2$O$_4$) nanostructure material and activated carbon derived from cocoa pod

Kabir O. Oyedotun, Abdulmajid A. Mirghni, Oladepo Fasakin, Delvina J. Tarimo, Vianney N. Kitenge and Ncholu Manyala*

Department of Physics, Institute of Applied Materials, SARChI Chair in Carbon Technology and Materials, University of Pretoria, Pretoria 0028, South Africa.

*Corresponding author's email: ncholu.manyala@up.ac.za

Abstract

Nickel-cobalt oxide (NiCo$_2$O$_4$) nano-agglomerates were effectively synthesized through a simplistic low temperature co-precipitation technique. The obtained material was further calcined to enhance its morphological properties and reduce the size of its individual particle of agglomerates. The as-synthesized NiCo$_2$O$_4$ agglomerates were characterized through the employment of various techniques, which include scanning/transmission electron microscopies (SEM/TEM), X-ray diffraction, Raman and X-ray fluorescence spectroscopies (XRF), and thermogravimetric analysis (TGA). Electrochemical performances of the as-synthesized electrode materials evaluated in a three-electrode configuration could deliver an optimized specific capacity of 95.6 mAh g^{-1} at 0.5 A g^{-1} specific current. of A fabricated hybrid asymmetric supercapacitor (SC) composed of the NiCo$_2$O$_4$ and the activated carbon obtained from cocoa pod (Cocoa AC-700) as positive and negative electrode (NiCo$_2$O$_4$//AC cocoa-700), respectively, delivered a specific capacity of around 168.7 mAh g^{-1} at 0.5 A g^{-1} and a corresponding specific energy and power of 47.7 Wh kg^{-1} 430.0 W kg^{-1}, respectively. The SC exhibited a substantial cycling stability resulting in a coulombic efficiency of 97.2 % with related capacity retention of 96.6 % recorded after a cycling test of over 11,000 cycles at 5 A g^{-1}.

Introduction

The emergence of compact electronic devices alongside electric and hybrid electric vehicles has earned supercapacitors popularity as alternative and complementary energy storage devices to batteries because of their high-power capability, high efficiency, quick charging and discharging ability and excellent cycling stability among others [1,2]. Of recent, research on rechargeable batteries such as lithium ion batteries has gained attention due to the need to develop energy storage devices for diverse mobile and stationary applications [1,2]. However, the demanding tasks remain evolving high-efficient, cost-effective, rechargeable, environmentally friendly, and safe solutions. Most of which seem to be satisfied by lithium-ion based batteries, one among the numerous available devices for electrochemical energy storage. The current subject of controversial debate remains whether the future demand for power sources can be achieved solely by the lithium-ion batteries.

Supercapacitors (SCs) also known as electrochemical capacitors (ECs) are a novel energy storage device, which can produce high power capabilities, significant cycle life, excellent stability and swift charge-discharge ability. They are potentially applicable in numerous fields, which include electric/hybrid electric and fuel cell vehicles, memory backup systems, flashlights, solar watches, remote controls and compact electronic devices amongst others [3–6]. Nevertheless, SCs applications are yet limited in real life owing to their low energy capability when contrasted with their lithium ion batteries counterpart [3]. SCs electrode materials play a crucial role in the devices' performances therefore, the investigation of auspicious materials with different nanostructures is currently a major rationale of supercapacitors' research.

Transition metal oxides, TMOs are representative electrode materials for electrochemical capacitors applications [3]. Besides, carbon materials (CMs) for instance activated carbon, carbon aerogels, carbon nanotubes as well as templated mesoporous carbon among others, are a kind of materials for fabricating electrodes for energy storage devices like supercapacitors. Both the TMOs and CMs are typically two kind of materials constituting two various charge storage mechanisms. The TMO materials show higher storage capability compared to CMs owing to the reversible Faradaic reactions. Unlike the TMOs, the CMs store electric charges through physical absorption by the emergence of an electric double layer (EDLC) at the electrode-electrolyte interface.

The combination of a battery-type positive electrode and a carbon negative electrode has been a feasible way with which hybrid SCs can be fabricated. This hybridization of two different kinds of materials could improve both the energy and power capabilities of the SC through provision of wider operating potentials along with higher capacitances/capacities [7,8].

Various efforts have been put in place to develop TMOs as electrocapacitive materials for use as positive electrodes in hybrid SCs owing to their abundance, cost-effectiveness, and scalable and facile synthesis/preparation properties [6–8]. The binary metal oxides in recent times, have fascinated a great curiosity from researchers by virtue of their possession of excellent electrical conductivity, variable and suitable oxidation states along with good thermal and chemical stabilities for enhanced electrochemical performances [7,8].

Transition metal oxides and/or hydroxides are semi-conductive materials. Among these materials are Ni- and Co-based oxides, which are being reckoned with as potential electrode materials' candidates for SCs application due to their cost effectiveness, natural abundance, high redox activities and ample electrochemical performances [6,9]. The latest progresses of NiCo-based materials application for energy storage devices have been reported in the literature [6,10–16].

These days, incessantly increasing depletion of fossil fuel and environmental pollution have resulted in drastic energy inadequacy, which makes it peremptory to search some clean and

renewable energy sources [17,18]. In this study, a hybrid asymmetric supercapacitor comprising a battery-type $NiCo_2O_4$ and a capacitor-type activated carbon derived from cocoa pod (Cocoa AC-700) materials as the positive and negative electrode, individually, was fabricated with a focus on $NiCo_2O_4$ electrode as the main study material. The binary-metal oxides electrode utilizing Ni and Co was synthesized by a facile low temperature co-precipitation technique. The adopted technique is a classical and perhaps the simplest means to synthesize metal oxide nanoparticles. As a kind of binary metal oxide, the $NiCo_2O_4$ has been largely explored and proved to have exhibited improved electrochemical performances compared to their corresponding individual metal oxide resulting from its higher theoretical capacitance, and more Faradaic redox reactions occurring at the its electrode-electrolyte [3,19–21]. The p-type semiconductor material, known for a band gap of 2.1 eV along with electronic conductivity of nearly a two-fold order of magnitude higher compared to Ni and Co oxides. The binary metal oxide material's morphology, structure, thermal ability alongside its electrochemical performances were cautiously investigated. The electrode investigated through a three-electrode system presented an optimum specific capacity 95.6 mAh g^{-1} at a specific current of 0.5 A g^{-1}. Furthermore, a fabricated asymmetric hybrid SC, $NiCo_2O_4$//AC cocoa-700 made up of the $NiCo_2O_4$ positive electrode along with the activated carbon derived from cocoa pod (Cocoa AC-700) as negative electrode proved a specific capacity of around 168.7 mAh g^{-1} founded on the device's total mass at 0.5 A g^{-1} and a corresponding peak specific energy of 47.7 Wh kg^{-1} at a specific power of 430.0 W kg^{-1}. The device displayed tremendous cycling stability, proving a coulombic efficiency of 97.2 % noted after a cycling test of over 11,000 cycles at a specific current of 5 A g^{-1}.

Experimental

The chemicals employed for material synthesis in this work were directly used as purchased with no further purifications.

Synthesis of NiCo₂O₄ nanostructured materials

The NiCo$_2$O$_4$ materials were typically synthesized as shown in Scheme 1, by dissolving 1 g each of Co(NO$_3$)$_2$.6H$_2$O with Ni(NO$_3$)$_2$.6H$_2$O salts in 100 mL of deionized (DI) water. Upon magnetic stirring, 2 g polyvinylpyrrolidone (PVP10-500G; mol. wt. 10,000) was added into mixture. The added PVP was adopted as a surfactant and for morphology control. Whilst stirring, 14 mL of 1 M NaOH was added drop wise into the solution for pH adjustment and to enhance polarity. Thereafter, the resulting mixture was left to stir at a rate of 400 rpm at 40 ˚C for 2h. After the process, the supernatant was poured out, and the obtained solid residue was centrifuged with ethanol and later with DI water. The idea of ethanol washing is to remove any surface attached PVP particles as well undissolved organic impurities from the sample. The recovered solid substance was put in an oven to dry overnight at 60 ˚C under ambient condition. The obtained powder sample, nickel cobalt binary hydroxide (NiCo-Bi(OH)) was then calcined at 200 ˚C in limited supply of air for 2h to further remove the associated moisture, volatile impurities and other organic matters from the sample, to have the final sample as NiCo$_2$O$_4$.
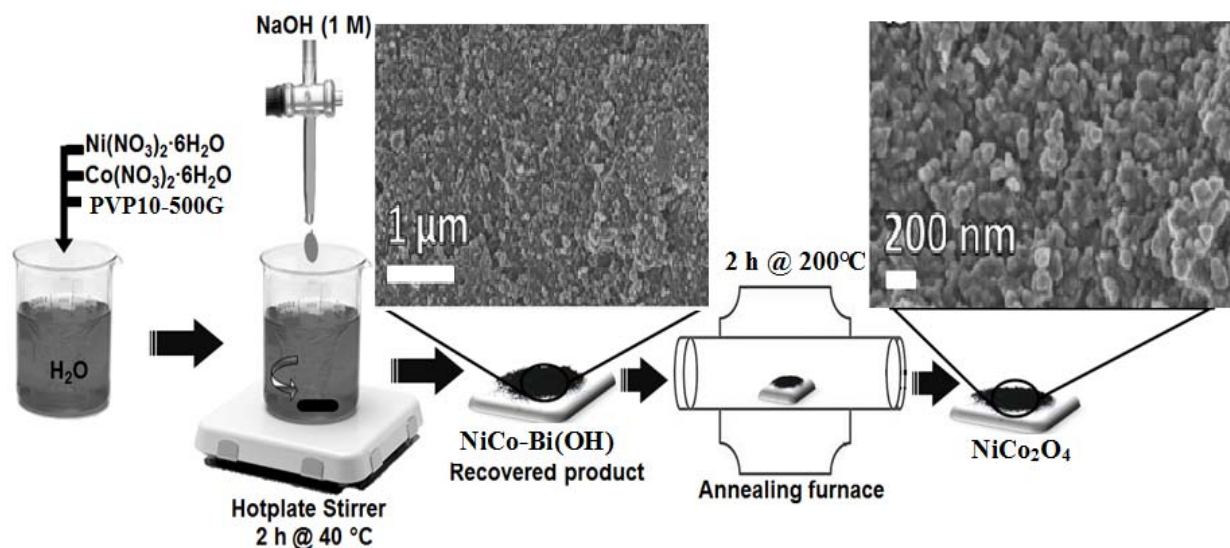
Scheme 1: Simplified representation of the synthesis route of NiCo$_2$O$_4$ nanoparticles.

Synthesis of activated carbon derived from cocoa pod (Cocoa AC-700)

The cocoa AC-700 adopted as negative electrode material in this work was synthesized by collecting waste pieces of dry cocoa pods from the farm. The collected waste cocoa pods were crushed, washed thoroughly with distilled water and then poured into a 120 mL Teflon-lined stainless-steel autoclave containing 100ml of distilled water in solution of 10 ml of 0.5M H_2SO_4. The added small volume of 0.5M H_2SO_4 was to remove organic impurities from the solution. Thereafter, the autoclave was closed up and transferred into an electric oven for hydrothermal process at 160 ˚C for 24 h. After the process, the recovered material was washed repeatedly with distilled water until pH of 7 was reached and dried overnight at 60 ˚C in an electric oven. The recovered dark powder sample was then added to potassium hydroxide (the activating agent) pellets in a mass ratio 1 (5 g) : 1 (5 g), muddled together in an agate mortal and moved into an atmospheric chemical vapour deposition (APCVD) set-up for further carbonization and activation at an optimized temperature of 700 ˚C and at a ramping rate of 5 ˚C/min in the flow of argon gas for a period of 2 h. After the process, the activated sample was first immersed in 3 M HCl solution to negate the effects of the remaining KOH particles in the substance and later washed severally with distilled water for neutrality. The resultant solid sample was dry overnight at 60 ˚C in an electric oven to have the final sample, which is designated as "Cocoa AC-700". A detailed study of the Cocoa AC-700 material utilized in the work was already in progress in our research group.

Material characterization

The as-prepared samples' micrographs were examined with the aid of a Zeiss Ultra Plus 55 field emission scanning electron microscope (FE-SEM) employed at 2.0 KV alongside a JEOL-2100F high-resolution transmission electron microscope (HRTEM FEI Tecnai-F30) utilized at 200 kV

acceleration potential. X-ray diffraction (XRD) review was obtained via the help of an XPERT-PRO diffractometer attached with the X'Pert HighScore Plus 3.0 (3.0.0) software for analysis (PANalytical BV, Netherlands), and reflection geometry at 2θ values (10–90°) alongside a step-size of 0.01°, and a Cu $K\alpha$ radiation source ($\lambda = 0.15418$ nm) at 50 kV and 30 mA. Raman analysis of the materials was done by utilizing a WITec alpha 300 RAS+ Confocal micro-Raman microscope (Focus Innovations, Germany) at a laser wavelength of 532 nm over a 120 s spectral accumulation time with a laser power of 5 mW. Thermal stability investigation of the samples was carried out by employing a DSC-TGA SDT Q600 V20.9 Build 20 thermogravimetric analyzer, utilized at a temperature range of 20 °C to 1000 °C in air and ramped a rate of 10 °C/min. XRF characterization of the sample, which was pressed prior to measurement was done through an ARL Perform'X Sequential XRF device and analyzed by a Uniquant software attached to the instrument. Analysis of the specific surface area (SSA) alongside pore size distribution (PSD) of cocoa AC-700 sample adopted as negative electrode in the study was carried out by employing a Quantachrome (NOVAtouch NT 2LX-1, Volts 220, USA) and analyzed via the Quantachrome TouchWin 1.22 Software that was attached to the system.

Electrochemical characterization

The electrodes used in this work were produced by adopting the as-prepared samples (80 wt%) as active material, with 10 wt% conductive acetylene black as conducting agent, and 10 wt.% polyvinylidene fluoride (PVDF) as binder. The materials were uniformly mixed together by addition of a few drops of N-methyl-2-pyrrolidone (NMP) solvent in a mortal and then blended to homogeneous slurry. The resulting slurry was plated on a 1 cm^2 nickel foam template adopted as current collector to make an electrode. The formed electrode was later dried at 70 °C over the night in an ambient oven. Electrochemical performances of the produced electrodes were investigated

using the Biologic VMP300 potentiostat (Knoxville TN 37,930, USA) accompanied with the EC-Lab® V1.40 software by means of a three- and two-electrode arrangement of measurement, respectively. Electrochemical assessments of the three-electrode testing were done by employing a glassy carbon as counter electrode, while the silver-silver chloride (Ag/AgCl) and as-prepared samples were employed as reference electrode and working electrode, respectively. All investigations were done by adopting 1 M KOH solution and at the room temperature (23 ˚C). The loading mass of active materials was determined as nearly 3.1 mg for all the three-electrodes and 4.8 mg for the two-electrode, respectively. The produced electrodes were investigated by utilizing cyclic voltammetry (CV) analysis, ran at distinct scan rates that range from 5 to 100 mV s^{-1} in an operating potential of 0.0 V to 0.43 V against Ag/AgCl reference electrode, and 5 to 100 mV s^{-1} and 0.0 V to 1.5 V, for both the half-cell and full cell, respectively. While galvanostatic charge-discharge, GCD analysis was done at distinct specific currents ranging between 0.5 and 10 A g^{-1} for the two set-ups, in a working potential ranging from 0.0 V to 0.42 V for the half-cell and 0.0 V to 1.5 V for the full cell. The samples' electrochemical impedance spectroscopy (EIS) was competently evaluated via the open-circuit potential at a range of frequencies between 10 mHz and 100 kHz.

The specific capacity, Q_s(mAh g^{-1}), of the electrodes (both the three- and two-electrodes) at a potential, E (V), as well as the coulombic efficiency, C_E of the nickel foam-underpinned electrode were estimated in line with the following equations:

$$Q_s = \frac{I_d \times \Delta t}{3.6} Q_s = \frac{I_d \times \Delta t}{3.6} \quad [\text{mAh g}^{-1}] \tag{1}$$

$$C_E = \frac{Q_{sd}}{Q_{sc}} \times 100\% C_E = \frac{Q_{sd}}{Q_{sc}} \times 100\% \tag{2}$$

where I_d is the specific current (in A g^{-1}), Δt is the electrode's discharge time (in s), and Q_{sc} and Q_{sd} are the specific capacities for the charge and discharge processes, respectively

Besides, the asymmetric device's specific energy and its corresponding power with respect to specific current were evaluated through the adoption of integral of the slope of discharge profile according to the relations:

$$E_d = I_d/3.6 \int Edt \quad \quad [\text{Wh kg}^{-1}] \tag{3}$$

$$P_d = 3.6 \times E_d/\Delta t \quad \quad [\text{Kw kg}^{-1}] \tag{4}$$

Q_s is electrode's specific capacity estimated according to the active material's effective mass. I_d is specific current (A g^{-1}). E is operating potential (V) of the cell, Δt is electrode's discharge time (s), Q_{sc} and Q_{sd} denote specific capacity for charge and discharge processes, while E_d and P_d denote specific energy and specific power, accordingly.

In addition, the masses between the separate electrode that made up the *SC* were accurately balanced by employing equation (5):

$$\frac{m_+}{m_-} = \frac{Q_{s-}}{Q_{s+}} \tag{5}$$

From equation (5), Q_s (mAh g^{-1}) symbolizes specific capacity of one electrode according to practical mass of active material, and *m* (g) indicates the active material's practical mass.

Results and discussion

SEM and TEM microscopies analysis

Figure 1 displays the SEM as well as TEM morphologies of the NiCo₂O₄ sample. Figure 1 (a and b) shows the SEM morphology/shape of the sample at low and high magnification, respectively. The observed randomly shaped nano-granular and aggregated particles fused together forming an irregular, nano grains structures that are varied in sizes and shapes. The morphology of the sample was additionally substantiated by adoption of TEM as revealed in Figure 1(c and d). The observed

TEM images evidently indicate agglomerated nano grain particles, which further corroborate what is noticed in SEM results already shown in Figure 1 (a and b).
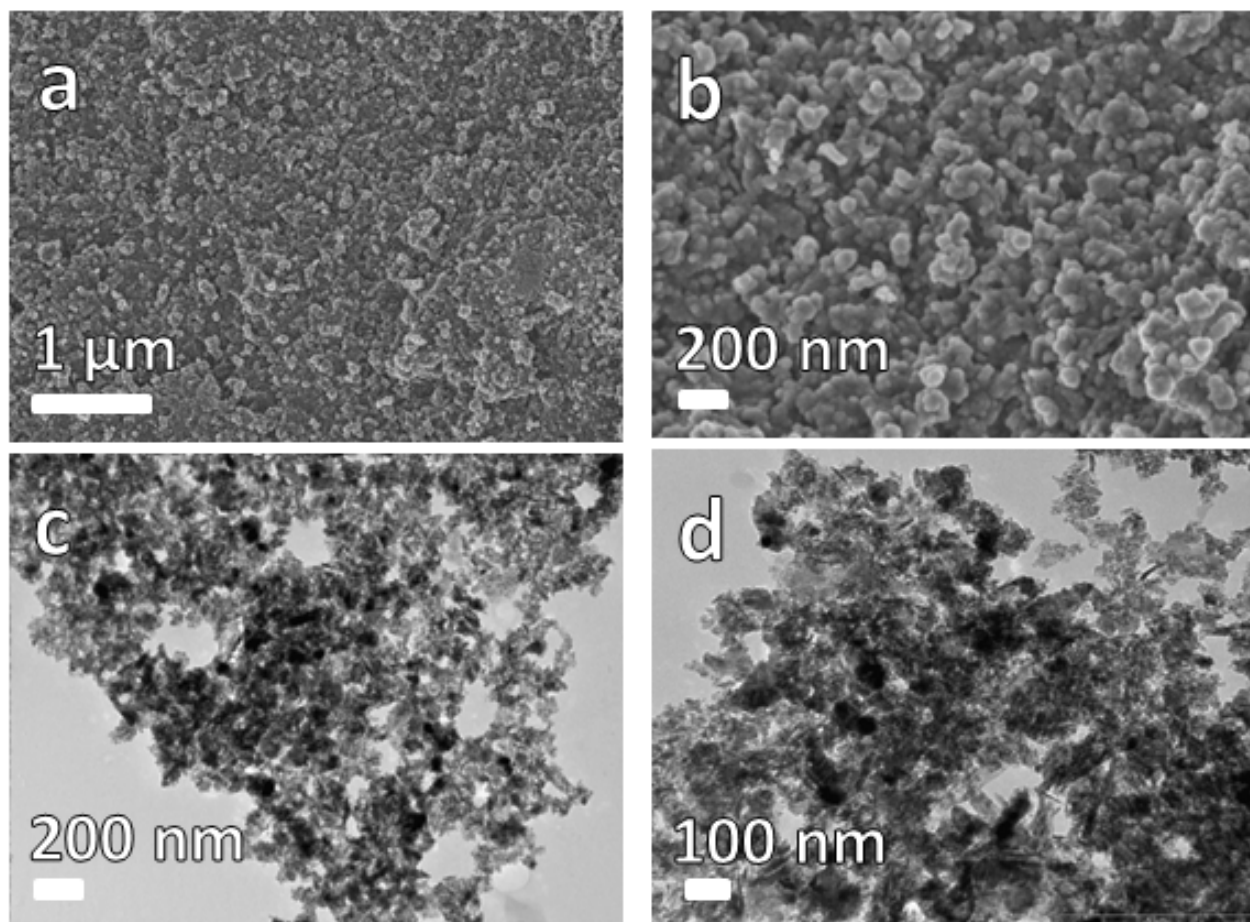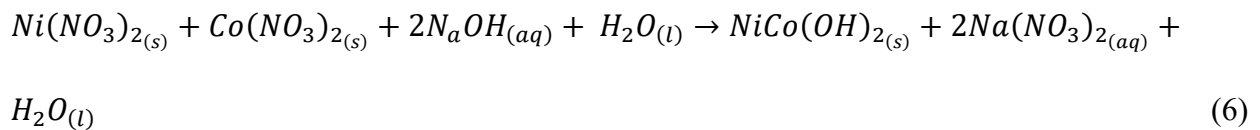

Fig. 1: (a-b) SEM images, and (c-d) TEM micrographs of $NiCo_2O_4$ at low and high magnifications, respectively.

Figure S1(a and b) in the supplementary document depicts the SEM images of the cocoa AC-700 material at different magnifications, respectively, adopted in this work as negative electrode. It can be shown that sample is composed of cavities with presence of many pores in the 3D interconnectivity strongly related within the structures of the sample [22].

Reaction kinetics mechanism of NiCo₂O₄ material

The co-precipitation technique adopted in this work entails a process in which metals are precipitated in form of hydroxides from their salt precursors through the aid of a base in a solvent. The technique involves a controlled release of anions and cations, which assists in regulating the nucleation as well as particle growth kinetics that helps in synthesizing monodispersed nanoparticles. The synthesized materials' form and particle size are controlled through nucleation and grain growth processes. Besides, time of reaction as well as temperature play an influential role in controlling the morphology and size corresponding to particle growth. The technique is adopted to attain a consistent composition in two or more cations homogeneous solution via the precipitation reaction that is one of determining techniques to synthesizing composites that have two or more sorts of metal elements. Scheme 2 provides a schematic diagram of the NiCo₂O₄ nanograins formation. The grown nanograin particles of NiCo₂O₄ from nuclei of NiCo₂O₄, further developed in size by following the Berthelot-Nernst law, resulting in homogeneous crystals. This is the case when diffusion in the interior is feasible (such as in the liquids) or when the initial small crystals can recrystallize. Kinetic effects such as speed of crystallization along with presence of mixing, play a crucial role. At the same time, owing to the high energy at the surface, the grains of the crystal self-assembled to give rise to an agglomerated structure of NiCo₂O₄ resulting from arranged growth along the vertical plane. The formed nanogranular structure of NiCo₂O₄ is interrelated to the inherent anisotropic property of the NiCo₂O₄ triagonal crystal structure. The following equation (6) outlines the reaction path to obtaining NiCo(OH)₂, which was further calcined as already shown in Scheme 1 to obtain the NiCo₂O₄ sample.

$$Ni(NO_3)_{2(s)} + Co(NO_3)_{2(s)} + 2N_aOH_{(aq)} + H_2O_{(l)} \rightarrow NiCo(OH)_{2(s)} + 2Na(NO_3)_{2(aq)} +$$

$$H_2O_{(l)} \tag{6}$$

The growth of these nanograin particles is the resultant of reagent reaction and kinetically controlled diffusion.
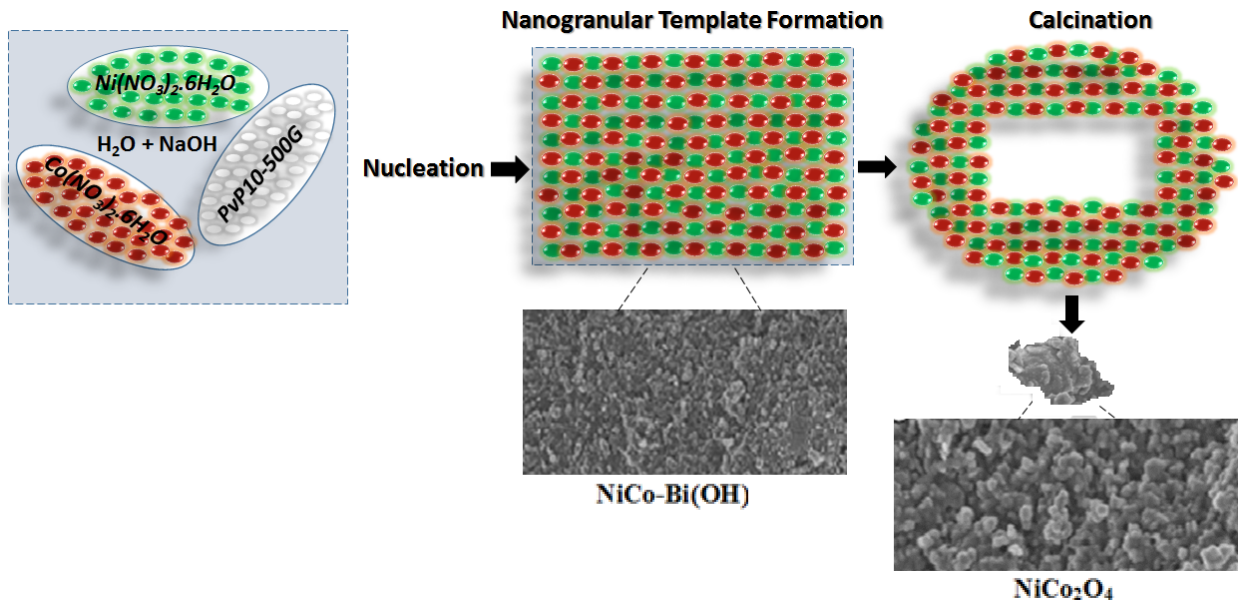
Scheme 2: An illustration of the mechanism of formation of $NiCo_2O_4$ nano material.

XRD, Raman and thermographic analysis

Figure 2 (a) is a representation of the XRD spectrum of the obtained $NiCo_2O_4$ electrode material. The observed pattern indicates strong diffraction peaks at 22.02°, 36.34°, 42.89°,44.90°, 52.33°, 57.44°, 65.38°, 69.90, 77.16°, 81.42˚, 82.82˚, and 88.41° 2θ values that are assigned to the (111), (220), (311), (222), (400), (331), (422), (511), (440), (531), (442), and (620) reflection planes, accordingly, which is in line with the identified ICSD Card no: 01-073-1702. The observed diffraction pattern of the as-as-synthesized sample validates that each lattice point has the face centered cubic structure.

Figure S1 (c) shows the XRD pattern of the activated carbon (cocoa AC-700). It can be observed that the sample is majorly composed of a high degree of amorphous owing to the rather broadened peak displayed at around 30.5º corresponding to the plane (002) indicating a high level of disorderliness in the sample. This is translating to the sample's higher degree of amorphous carbon state. Figure 2 (b) is display of the $NiCo_2O_4$ sample's typical Raman spectrum. Vibrational modes of the nanoparticles were noticed at around 76, 337, 509, and 1028 cm^{-1}, which agree with

the F2g, Eg, LO as well as 2 LO modes of the $NiCo_2O_4$, respectively. The noticed results are in agreement with those recorded in previous reports [23–25]. Figure S1 (d) depicts the Raman analysis of the cocoa AC-700. The Figure displays the signatory D- and G-peaks positioned at a wavenumber of approximately 1341 and 1589 cm^{-1}, respectively, indicating a high structurally disordered 3D carbon material [26,27]. The D and G peaks are attributed to defect and graphitization of the sample, respectively. The presence of G bands as observed in the Raman spectra in Figure 2 (b) shows the existence of graphitic carbon in the synthesized electrode materials.
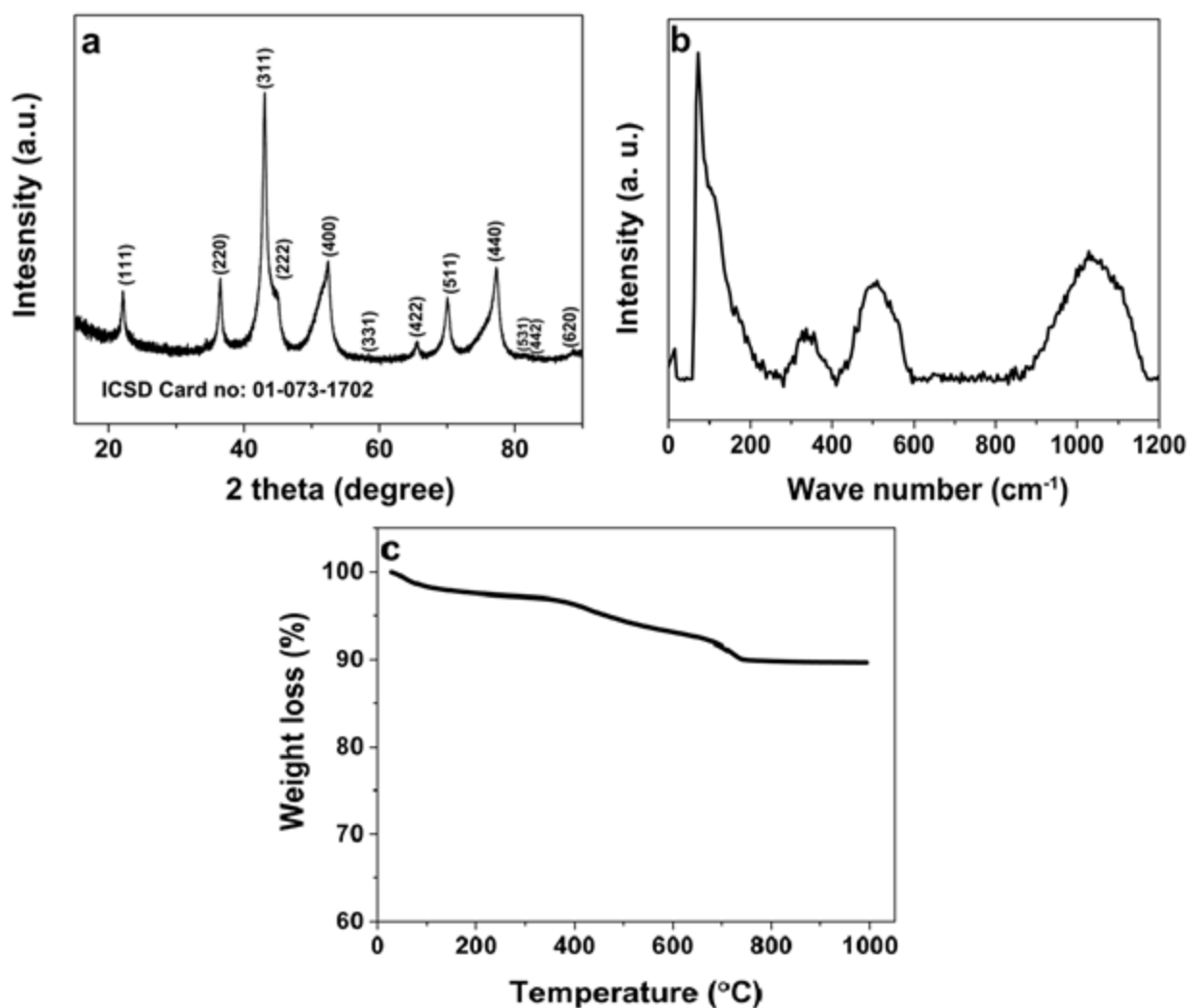

Fig. 2: (a) XRD pattern and the matching ICSD card number, (b) Raman spectrum, (c) TGA analysis of $NiCo_2O_4$ sample, respectively.

Figure 2 (c) demonstrates the TGA profile for the $NiCo_2O_4$ nanostructure with an initial sample size of ~ 18.40 mg prior to the analysis. From 2 (c), an observed weight loss at 26.97 ˚C – 285.95 ˚C (2.820 %; 0.519 mg; residue: 97.18 % (17.88 mg)) is as a result of the decomposition of the binary metal into the discrete oxides [28]. The weight loss at about 285.95 ˚C - 601.36 ˚C (4.151 %; 0.764 mg; residue: 93.02 % (17.12 mg)) is ascribed to loss of interfacial adsorbed moisture in the sample. The detected weight loss at around 601.36 °C – 990.56 ˚C (3.358 %; 0.618 mg) is a demonstration that the adsorbed water molecules have evaporated with further decomposition of the binary metal oxides. Due to the remaining weight of the material; 89.67 % (16.50 mg) at about 990.56 °C, the quantity of C substance held in the composite was estimated as about 10.33 wt.%. In the material, various decomposition temperatures were noticed owing to loss of adsorbed water. At around 730.56 – 990.56 °C, the weight of the substance was observed to be nearly consistent indicating a stable binary metal oxide as regards to thermal stability.

As depicted in Table 1, a weight % ratio of ~ 1:1:0.7 was revealed for the Ni:Co:O in the composite sample through the aid of the XRF device's Uniquant software adopted to examine every element in the periodic table between Na and U, with only elements detected over the limit of detection being described. The values were normalized, as no loss on ignition (LOI) was performed to ascertain changes in crystal water and oxidation state. The existence of Na in notable quantity (1.03 wt. %) is attributed to the adoption of 1 M NaOH for sample preparation in the laboratory, while presence of other trace elements is due to impurities from the chemicals employed in material preparation.
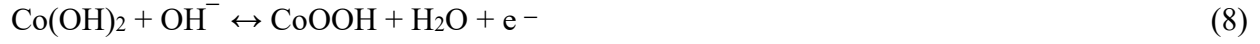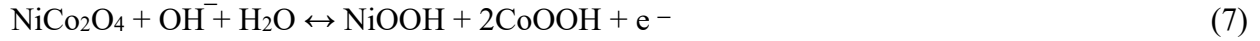
Table 1. Showing XRF analysis of as-synthesized $NiCo_2O_4$ nanocomposite.

Compound	Weight %
Co	36.46
Ni	37.65
Na	1.03
Si	0.34
Mg	0.10
Sx	0.02
Cu	0.02
Al	0.01
Ca	0.01
O	24.34
TOTAL	**99.99**

Loss on ignition = 0.01 Weight %.

Electrochemical investigation

Electrochemical evaluations of the as-produced electrodes were investigated by adopting both the three- and two-electrodes systems. All electrochemical investigations were carried out by utilizing 1 M KOH solution as the electrolyte. Fig. 3(a) depicts the obtained CV curves of $NiCo_2O_4$ material via a three-electrode measurement within a scan rate ranging from 5 mV s^{-1} to 100 mV s^{-1} and at a maximum operating potential of ~ 0.43 V. The non-rectangular CV curves with clear Faradaic behavior portrays that the electrode possesses a high current response indicating a record specific capacity. In Fig. 3(b), a plot of the associated GCD curves of the electrode at distinct specific currents and a maximum operating potential of ~ 0.43 V was displayed. The clear potential steps observed from the electrode's GCD profiles affirms the Faradic behavior of the material, which further confirms the CV curves in Fig. 3(a). The noticed nonlinear CV and GCD profiles depict clear oxidation along with reduction peaks at about 0.1 V and 0.3 V suggesting the anodic and cathodic peaks, proportionately, triggering the reversible Faradaic reactions owing to a varied composition containing Ni^{2+}, Ni^{3+} and Co^{3+}, Co^{4+} in the material [6]. The observed redox reactions in the material can be expressed according to the following relations [29]:

$$NiCo_2O_4 + OH^- + H_2O \leftrightarrow NiOOH + 2CoOOH + e^- \tag{7}$$

$$Co(OH)_2 + OH^- \leftrightarrow CoOOH + H_2O + e^- \tag{8}$$

$$CoOOH + OH^- \leftrightarrow CoO_2 + H_2O + e^- \tag{9}$$

The electrical resistance of the $NiCo_2O_4$ electrode was further estimated by conducting its electrochemical impedance spectroscopy (EIS) at a potential of 0.0 V and a frequency range of 10 mHz –100 kHz. Fig. 3(c) represents the Nyquist plot of the electrode, showing a distinct semicircle (inset to Fig. 3(c)) in the high frequency region. The noticed semicircle is ascribed to the interfacial charge transfer resistance along with mass transport across the material [6]. From the figure, the overall resistance of the electrolyte's ionic resistance, active materials' intrinsic resistance and the contact resistance at the interface between the current collector and active electrode material, (R_S) is estimated to be ~ 0.62 Ω. The very low R_S value observed for the material suggests its high conductivity. The estimated specific capacities of the single electrode by employing equation 1 is plotted with respect to distinct specific currents as represented in Fig. 3 (d). The $NiCo_2O_4$ electrode proved a peak specific capacity of 95.6 mAh g^{-1} at a specific current of 0.5 A g^{-1} and was able to still maintain a specific capacity of 44.7 mAh g^{-1} even at a peak specific current of 10 A g^{-1}.
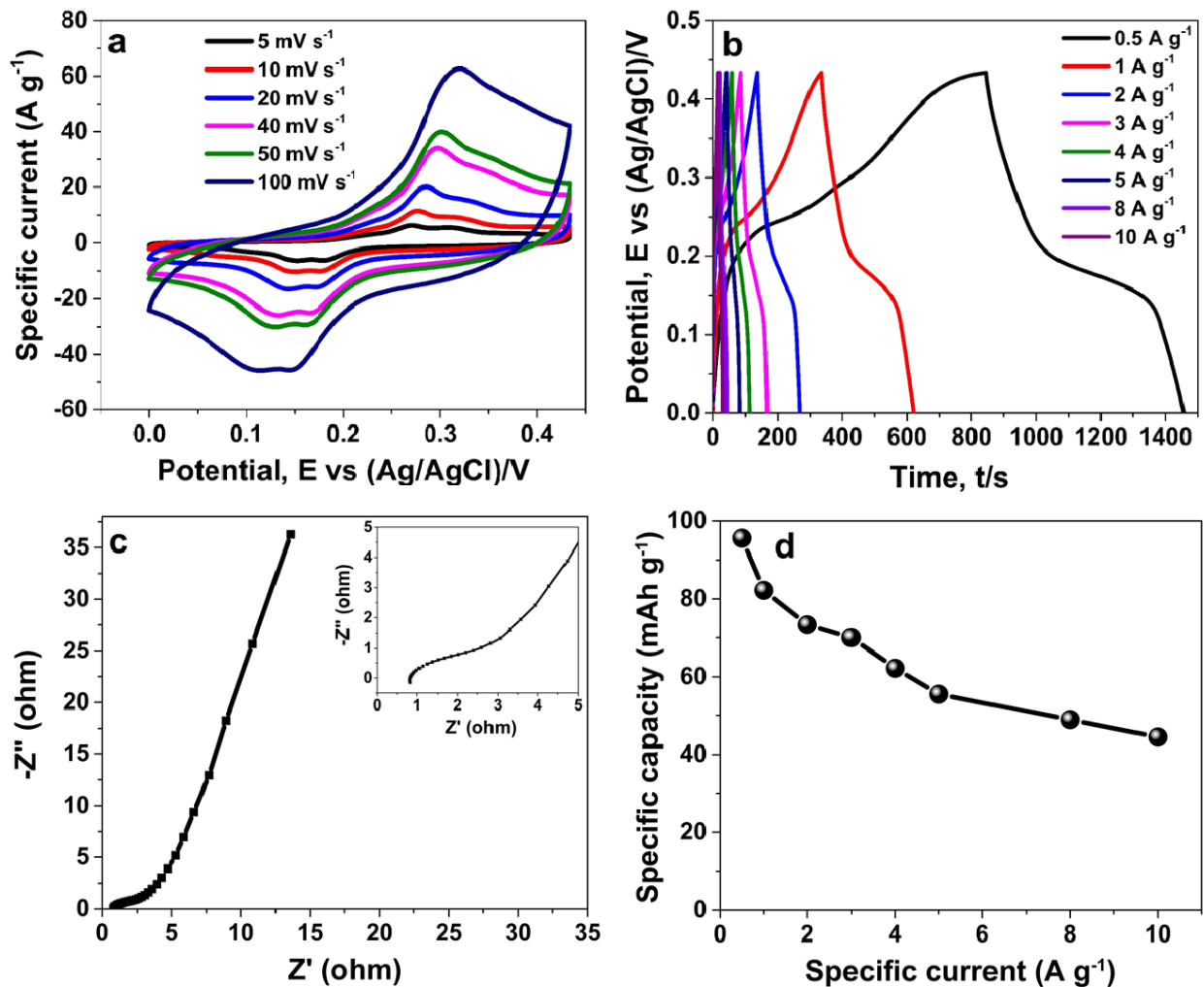
Fig. 3: (a) CV curves and (b) GCD profiles at distinct scan rates and specific currents, (c) Nyquist impedance plot for the sample, and (d) specific capacitance calculated for the NiCo$_2$O$_4$ sample at various scan rates, respectively.

As a battery-type material, the NiCo$_2$O$_4$ electrode capacitive contributions were calculated to better understand electrochemical energy storage mechanism of the material. The ions diffusion and surface charge adoption (capacitive) are two crucial processes controlling material's charge storage mechanism. At elevated scan rates, diffusion process of the ions is observed to be predominant, while the capacitive process prevails at low scan rates. From the CV profiles in

Figure 3 (a), the current (I) dependence with respect to the scan rate (v) can be evident for the two processes in line with the following equations [30-33]:

$$I = av^b \qquad\qquad 10$$

which can also be written as:

$$\log i = b \log v + \log a \qquad\qquad 11$$

The capacitive as well as diffusion I_S and I_D governed currents, respectively, can be related as:

$$I_S = k_1 v \qquad\qquad 12$$

$$I_D = k_2 v^{1/2} \qquad\qquad 13$$

where a, b, k_1 and k_2 are constants.

The total current, I, resulting from equations 12 and 13 can be written as:

$$I = I_S + I_D \qquad\qquad 14$$

$$\frac{I}{v^{1/2}} = k_1 v^{1/2} + k_2 \qquad\qquad 15$$

Equation 15 can be demonstrated as a straight-line equation having k_1 and k_2 as the slope and intercept, respectively. Figure 4 (a) shows the material's peak currents with respect to the square roots of the distinct scan rates ($v^{1/2}$) estimated as stated in equation 15. The Figure reveals a linear correspondence of peak currents in contrast to square roots of the scan rates as inferred by adoption of the OriginPro 9.0 64-bit software. The noted linear relationship associated with the anodic oxidation as well as cathodic reduction peaks showing the R^2 values of approximately 0.99 substantiates that the material exhibits a diffusion controlled electrochemical reaction. This indicates an increased assertion of swift Faradaic charge storage activities occurring within the NiCo$_2$O$_4$ electrode [13]. The fractional values of capacitive and diffusion charge toward the contribution of the obtained current, estimated at various scan rates and in line with equations 11

and 12, are displayed in Figure 4 (b). At low scan rate (5 mV s^{-1}), the diffusion contribution is noticed to be around 24.5 %, which improves to 76.5 % at an elevated scan rate of 100 mV s^{-1}. A reversed pattern could be observed for the capacitive associated contribution. The observed prominent diffusion charge contribution at high scan rates indicates that the electrolyte ions are efficiently diffused within the electrode's pores.
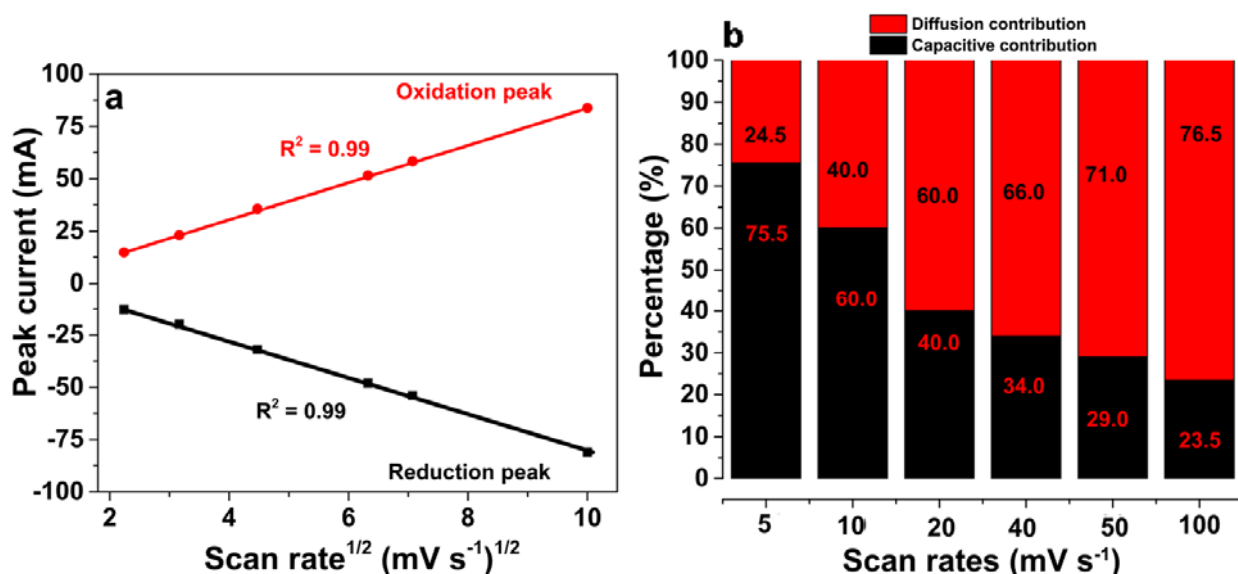

Fig. 4. (a) Variation of peak currents versus square root of scan rates, and (b) capacitive and diffusion contributions estimated at various scan rates for the NiCo$_2$O$_4$ material electrode.

Fig. S3 (a) in the supporting document, shows the electrochemical capability of the Cocoa AC-700 electrode at various scan rates via a three-electrode system. The negative electrode material indicated no observable peaks in its profiles but a perfect rectangular CV profiles, attesting the electrode's double-layer capacitive properties with adequate reversibility. Fig. S3 (b) exhibits the GCD profiles of the Cocoa AC-700 negative electrode at different specific currents. The electrode material reveals a specific capacitance of ~ 172.2 F g^{-1} at 0.5 A g^{-1}, calculated according to equation SE 1 *(see supporting document)*. Fig. S3 (c) is a display of the Cocoa AC-700 electrode's Nyquist plot. The plot is observed to be composed of a near Warburg line within

the low frequency region and a semicircle within the high frequency region with an corresponding series resistance (R_s) of nearly 0.8 Ω specifying a typical capacitive response of EDLC electrodes.
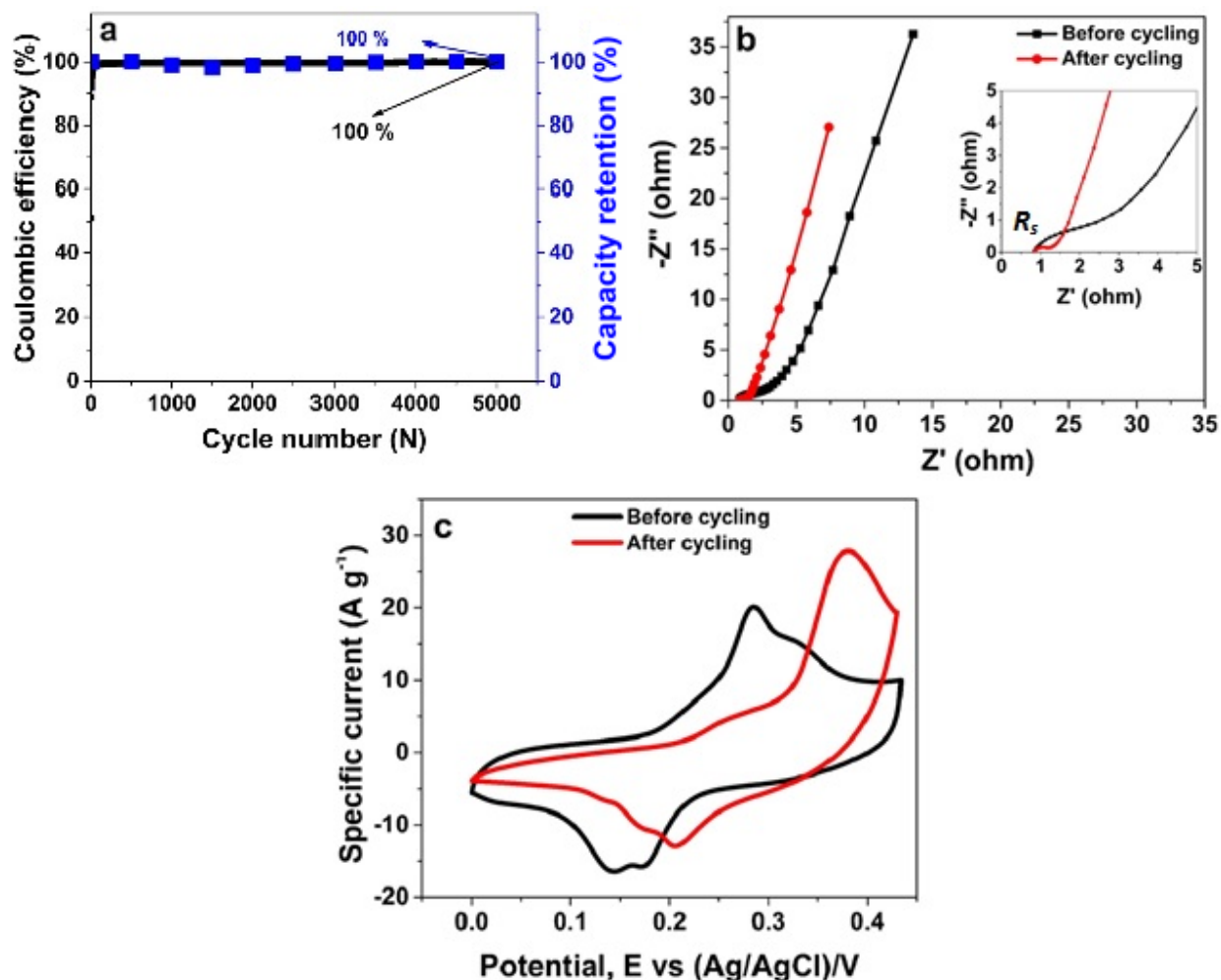

Fig. 5. (a) Distinctions of capacity retention and coulombic efficiency of $NiCo_2O_4$ electrode against cycle numbers examined at 5 A g^{-1} in 1 M KOH, (b) Nyquist plot prior to and following the 5000 charge and discharge cycles at 5 A g^{-1}, and (c) CV profiles prior to and over 5000 charge and discharge cycles for the $NiCo_2O_4$, respectively.

Fig. 5(a) shows coulombic efficiency along with percentage specific capacity retention plotted against cycle numbers over repeated 5000 charge/discharge cycles for the $NiCo_2O_4$ electrode at a specific current of 5 A g^{-1}. A significant coulombic efficiency as well as specific capacity retention of ~ 100 %, respectively, was revealed by the electrode after the repeated charge-

discharge test, which further demonstrates the high feasibility of the material's redox process. Fig. 5(b and c) shows the EIS Niquist plots and CV profiles (at a scan rate of 20 mV s^{-1}) of NiCo$_2$O$_4$ electrode taken before and after the 5000 charge-discharge cycles test. In Fig. 5 (c), it could be noticed that the current output for the electrode after the cycling test slightly improved. This improvement in current response can be correlated to the lower solution resistance of ~ 0.60 Ω shown for the electrode in the high frequency region against the 0.62 Ω (before cycling) noticed as suggested by Fig. 5(b) and the inset.

Figure 6 (a and b) depicts the NiCo$_2$O$_4$ electrode's SEM images at low and high magnifications that were taken following the cycling test of about 5000 cycles. The electrode shows no remarkable change in morphology, in contrast to the images in Figure 1 (a and b) despite the long-term cycling, which infers the sample's good electrochemical and structural stabilities.
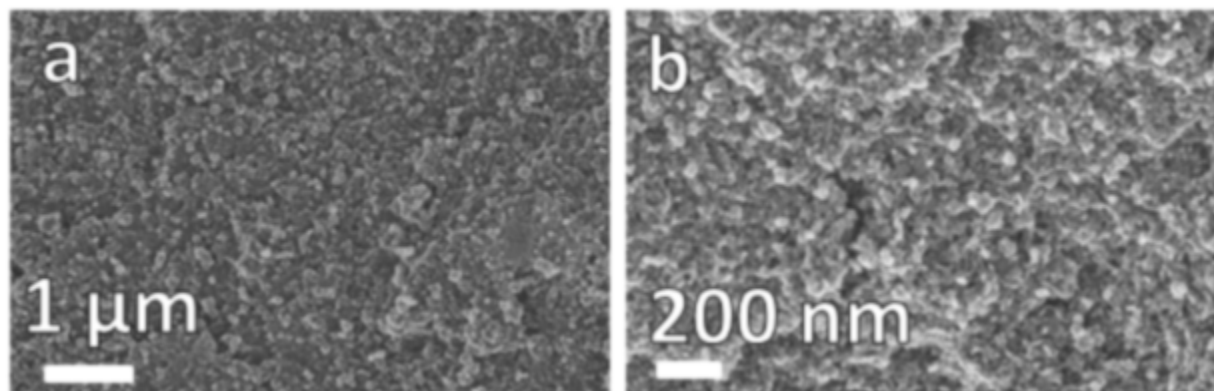

Fig. 6. (a and b) SEM images of NiCo$_2$O$_4$ material following the cycling of 5000 cycles at 5 A g^{-1} in 1 M KOH electrolyte.

Electrochemical analysis of hybrid NiCo$_2$O$_4$//Cocoa AC-700 two-electrode cell

On account of the significant electrochemical properties of both the NiCo$_2$O$_4$ and AC cocoa-700 adopted as positive and negative electrode, separately, an asymmetric SC was then assembled to achieve a hybrid device that is capable of improved performances by integrating the features of

traditional SCs with those of batteries. The fabricated hybrid supercapacitor in this case is designated as $NiCo_2O_4$//Cocoa AC-700. The mass balance ratio of the device was achieved in line with equation 5 and estimated as ~ 1.8:3.0 for the $NiCo_2O_4$ and Cocoa AC-700 electrode, separately. The hybrid device working electrode was produced through the muddling of the active material with carbon acetylene black (CAB) and polyvinylidene difluoride (PVDF) at a weight ratio of 80:10:10, respectively, in a few drops of 1-Methyl-2-pyrrolidinne (NMP) to form homogeneous slurry. The added CAB and PVDF serve as conducting agent and binder, respectively. The produced slurry was later pasted onto 1.5 cm Ө disc-like Ni foam support, which serves as current collector and then dried at 60 °C over the night in atmospheric condition. The estimated whole mass loading of active material in the hybrid device's electrodes was ~ 4.8 mg, while the thickness of the electrode estimated via the employment of micro balance was nearly 96 μm.

Fig. 7 (a and b) is a manifestation of the CV and GCD profiles examined in a three-electrode configuration for both the $NiCo_2O_4$ and Cocoa AC-700 adopted as positive and negative electrode, separately. The observed supposedly rectangular CV/GCD curve for the Cocoa AC-700 as shown in Fig. 7 (a and b) is somewhat like the double-layer capacitive behaviours, while the non-linear CV/GCD curve for the $NiCo_2O_4$ electrode is an indication of a typical Faradaic behavior as a result of the redox reactions occurring through the charge and discharge processes. It can be observed (see Fig. 8 (a)) that the assembled asymmetry device could perform well in a much wider potential of around 1.5 V, which is as a result of combined effect of the individual electrode's working potentials.
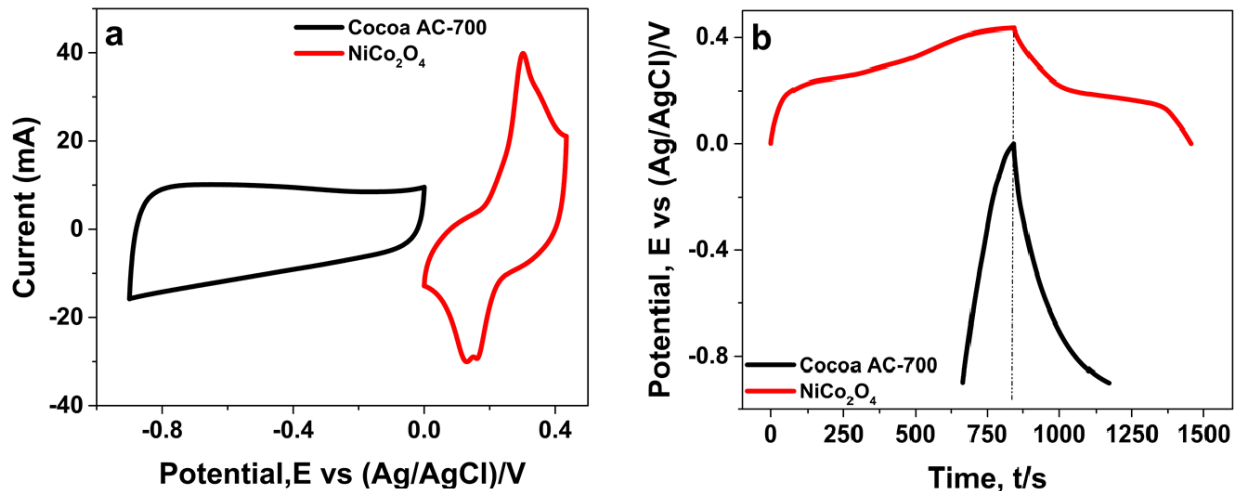
Fig. 7. (a) CV curves at 50 mV s^{-1}, and (b) CD curves at 1 A g^{-1} of NiCo$_2$O$_4$ and AC cocoa-700, respectively.

Fig. 8 (a) reveals the NiCo$_2$O$_4$//AC cocoa-700 hybrid device's CV curves taken at respective scan rates in the range of 5 to 100 mV s^{-1}, while Fig. 8 (b) is a display of its comparable GCD profiles recorded at respective specific currents. The observed non-linear CV and GCD profiles at different scan rates and specific currents, respectively, are a signature of mixed Faradaic and EDLC properties, which is a representative of asymmetric hybrid supercapacitors [6]. The equicrural triangular GCD profiles as shown in Fig. 8 (b), are substantially non-symmetrical specifying the synergy between the NiCo$_2$O$_4$ and AC cocoa-700 materials that is in line with the CV profiles observed for the device as depicted in Fig. 8 (a). Fig. 8 (c) manifests specific capacities of the asymmetric device evaluated at distinct specific currents and by using equation 1 via the GCD profiles. The device could deliver a peak specific capacity of ~ 168.7 mAh g^{-1} based on its whole mass at a specific current of 0.5 A g^{-1}. The Nyquist plot of the NiCo$_2$O$_4$//AC cocoa-700 SC prior to and following the cycling test of over 11,000 GCD cycles was analyzed and presented as shown in Fig. 8 (d). The slight equivalent series resistance, R_s in the high-frequency region of the electrochemical system was estimated to be ~ 3.68 Ω cm^{-2} and 3.85 Ω cm^{-2} for before and after the

23

cycling test, respectively, indicating the supercapacitor's good conductivity, which is not affected by the stability tests. Fig. 8 (e) indicates the cell's plot of coulombic efficiency evaluated according to equation 2, and its percentage capacity retention plotted against the cycle numbers for over 11,000 cycles. From the Figure, a remarkable coulombic efficiency of about 98.9 % as well as a capacity retention ability of nearly 96.6 % of its initial specific capacity was recorded for the hybrid device over a repeated GCD test of 11,000 cycles at 5 Ag^{-1}. The manifested high cycling stability of the asymmetric SC further demonstrates its redox process's high feasibility. The hybrid SC electrode materials did not encounter any consequential structural defectiveness of the electrode materials during long period of cycling. This is attributed to the remarkable cavities with the existence of a fairly large number of pores in a 3D interconnection closely related within the AC cocoa-700 material's structures *(see Fig. S1(a and b) in supplementary document)*. The high capacity retention exhibited by the device is an attribute of a high electronic conductivity, owing to the particular porous structure as well as high specific surface area, SSA (836 m^2 g^{-1}) of the AC cocoa-700 *(see Figure S2 (a and b in supplementary document)*, which makes the material much more available to ion diffusion within the pores of the 3D interconnection connected together in the frameworks of the material. The high SSA of the sample along with its pore-size distribution (PSD) are advantageous in charge storage through the supplying of superb adsorbate accessibility with large flow routes to micropores [4,34]. Besides, the electrochemical responses are generally determined by the insertion and extraction of OH$^-$ from the electrolyte whilst the porous structure of AC cocoa-700 is instrumental in the diffusion of ions into the electrode holes [4,35].

Fig. 8 (f) shows the *SC*'s Ragone plot, indicating a peak specific energy of 47.7 Wh kg^{-1} corresponding to a specific power of 430.0 W kg^{-1} estimated by using equation 3 and 4, accordingly, at a 0.5 A g^{-1} specific current.
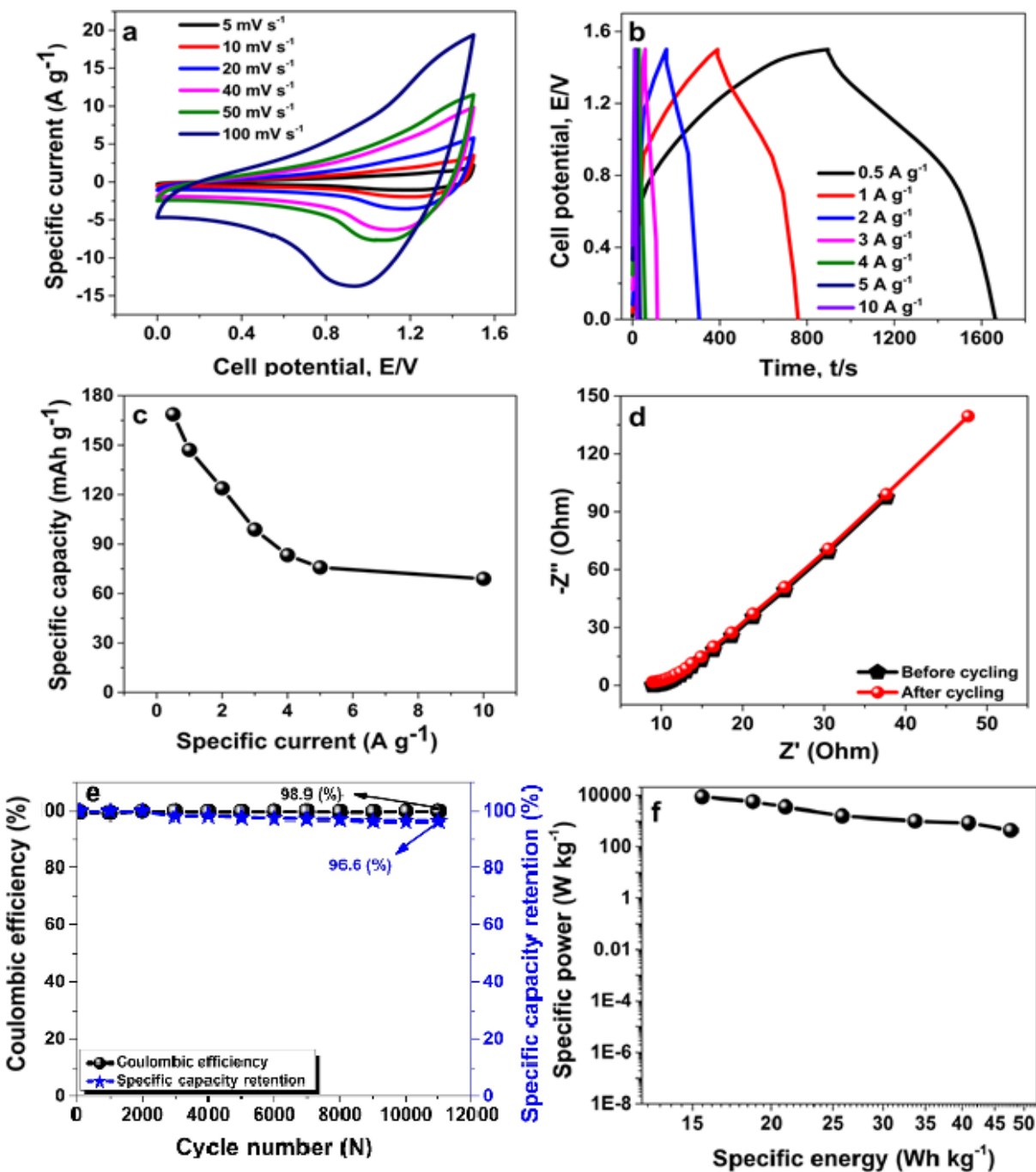
Fig. 8. (a) CV profiles at various scan rates, (b) GCD profiles at various specific currents, (c) specific capacity against specific currents (d) Nyquist plot prior to and following 11000 charge-discharge cycles at a specific current of 5 A g^{-1}, (e) coulombic efficiency and capacity retention at 5 A g^{-1} in 1 M KOH, and (f) Ragone plot of the asymmetric NiCo$_2$O$_4$//AC cocoa-700 cell.

The displayed estimates for specific energy and power along with percentage capacity retention by the NiCo₂O₄//AC cocoa-700 device in this study as depicted in Figure 8 (e and f), have substantial improvement when compared to other similar NiCo₂O₄//AC devices in aqueous electrolytes. Such devices are exhibited in Table 1. The selected work the Table were of distinct regard due to their distinguished electrochemical behaviors. Such behaviours as extended device's operating potential, higher specific capacity/capacitance and remarkable cycle stability.

Table 2: Electrochemical properties of similar NiCo₂O₄//AC devices drawn out from the literature.

Device	Electrolyte	Specific energy (Wh kg⁻¹)	Specific power (W kg⁻¹)	Cycling stability	Reference
NiCo₂O₄/MnO₂//Biochar	6 M KOH	30.4	133.5	88% over 5000 cycles	[19]
NiCo₂O₄ nanospheres//AC	1 M KOH	21.5	750	87.8% over 2000 cycles at 5 A g⁻¹	[20]
NiCo₂O₄/Ni0.85Se//AC	1 M KOH	29.3	99	83.2% over 5000 cycles at 5 A g⁻¹	[36]
NiCo₂O₄/CoFe LDH//AC	2 M KOH	28.9	950	76.9% over 5000 cycles at 2 A g⁻¹	[21]
NiCo₂O₄/NiWO₄//AC	6 M KOH	41.5	760	N/A	[37]
NiCo₂O₄/NiO//AC	2 M NaOH	47.4	389	81.4% over 2000 cycles	[38]
NiCo₂O₄@α-Co(OH)₂//AC	2 M KOH	39.7	387.5	83% over 5000 cycles at 2 A g⁻¹	[3]
NiCo₂O₄//Cocoa AC-700	1 M KOH	47.7	430	96.6% over 11000 cycles at 5 A g⁻¹	This work

CONCLUSIONS

$NiCo_2O_4$ and activated carbon derived from waste cocoa pod (AC cocoa-700) electrode materials were well synthesized via a facile low temperature co-precipitation technique and atmospheric pressure chemical vapour deposition (APCVD) technique, respectively. Various characterization techniques adopted revealed that the as-synthesized binary metal oxide material possesses nano-agglomerated and non-uniform grain particles compared to the porous 3D interconnected and closely linked structures morphology observed for the AC cocoa-700 material. Electrochemical performances of the as-synthesized $NiCo_2O_4$ evaluated in a three-electrode system could deliver an optimized specific capacity 95.6 mAh g^{-1} at 0.5 A g^{-1}. A fabricated asymmetric hybrid SC, $NiCo_2O_4$//AC cocoa-700 composed of the $NiCo_2O_4$ positive electrode alongside the activated carbon derived from cocoa pod (Cocoa AC-700) negative electrode proved a specific capacity of around 168.7 mAh g^{-1} based on the device's whole mass at 0.5 A g^{-1} and a corresponding peak specific energy of 47.7 Wh kg^{-1} at a specific power of 430.0 W kg^{-1}. The device exhibited a superb cycling stability alongside a coulombic efficiency of 97.2 % noted after a cycling test of over 11,000 cycles at 5 A g^{-1}. The device's excellent performances reveal that composite materials could be a potential for methodical electrodes for electrochemical energy storage devices applications.

References

(1)   Yan, D.; Wang, W.; Luo, X.; Chen, C.; Zeng, Y.; Zhu, Z. NiCo2O4 with Oxygen Vacancies as Better Performance Electrode Material for Supercapacitor. *Chem. Eng. J.* **2018**, *334*, 864–872. https://doi.org/10.1016/j.cej.2017.10.128.

(2)   Xia, C.; Chen, W.; Wang, X.; Hedhili, M. N.; Wei, N.; Alshareef, H. N. Highly Stable Supercapacitors with Conducting Polymer Core-Shell Electrodes for Energy Storage Applications. *Adv. Energy Mater.* **2015**, *5* (8), 1401805. https://doi.org/10.1002/aenm.201401805.

(3)   Wang, W. D.; Zhang, P. P.; Gao, S. Q.; Wang, B. Q.; Wang, X. C.; Li, M.; Liu, F.; Cheng, J. P. Core-Shell Nanowires of NiCo2O4@a-Co(OH)2 on Ni Foam with Enhanced Performances for Supercapacitors. **2020**, *579*, 71–81. https://doi.org/10.1016/j.jcis.2020.06.048.

(4)   Oyedotun, K. O.; Barzegar, F.; Mirghni, A. A.; Khaleed, A. A.; Masikhwa, T. M.; Manyala, N. Examination of High-Porosity Activated Carbon Obtained from Dehydration of White Sugar for Electrochemical Capacitor Applications. *ACS Sustain. Chem. Eng.* **2019**, *7* (1), 537–546. https://doi.org/10.1021/acssuschemeng.8b04080.

(5)   Oyedotun, K. O.; Masikhwa, T. M.; Lindberg, S.; Matic, A.; Johansson, P.; Manyala, N. Comparison of Ionic Liquid Electrolyte to Aqueous Electrolytes on Carbon Nanofibres Supercapacitor Electrode Derived from Oxygen-Functionalized Graphene. *Chem. Eng. J.* **2019**, *375*, 121906. https://doi.org/10.1016/j.cej.2019.121906.

(6)   Oyedotun, K. O.; Madito, M. J.; Momodu, D. Y.; Mirghni, A. A.; Masikhwa, T. M.; Manyala, N. Synthesis of Ternary NiCo-MnO 2 Nanocomposite and Its Application as a Novel High Energy Supercapattery Device. *Chem. Eng. J.* **2018**, *335*, 416–433. https://doi.org/10.1016/j.cej.2017.10.169.

(7)   Huang, Y. Y.; Lin, L. Y. Synthesis of Ternary Metal Oxides for Battery-Supercapacitor Hybrid Devices: Influences of Metal Species on Redox Reaction and Electrical Conductivity. *ACS Appl. Energy Mater.* **2018**, *1* (6), 2979–2990. https://doi.org/10.1021/acsaem.8b00781.

(8)   Vlad, A.; Singh, N.; Rolland, J.; Melinte, S.; Ajayan, P. M.; Gohy, J. F. Hybrid Supercapacitor-Battery Materials for Fast Electrochemical Charge Storage. *Sci. Rep.* **2014**, *4*, 1–7. https://doi.org/10.1038/srep04315.

(9)   Feng, L.; Zhu, Y.; Ding, H.; Ni, C. Recent Progress in Nickel Based Materials for High Performance Pseudocapacitor Electrodes. *J. Power Sources* **2014**, *267*, 430–444. https://doi.org/10.1016/j.jpowsour.2014.05.092.

(10)   Deng, T.; Zhang, W.; Arcelus, O.; Kim, J.-G.; Carrasco, J.; Yoo, S. J.; Zheng, W.; Wang, J.; Tian, H.; Zhang, H.; Cui, X.; Rojo, T. Atomic-Level Energy Storage Mechanism of Cobalt Hydroxide Electrode for Pseudocapacitors. *Nat. Commun.* **2017**, *8*, 15194. https://doi.org/10.1038/ncomms15194.

(11)   Pan, Z.; Qiu, Y.; Yang, J.; Ye, F.; Xu, Y.; Zhang, X.; Liu, M.; Zhang, Y. Ultra-Endurance Flexible All-Solid-State Asymmetric Supercapacitors Based on Three-Dimensionally Coated MnOx Nanosheets on Nanoporous Current Collectors. *Nano Energy* **2016**, *26*,

610–619. https://doi.org/10.1016/j.nanoen.2016.05.053.

(12)   Wang, H. X.; Zhang, W.; Drewett, N. E.; Zhang, H. B.; Huang, K. K.; Feng, S. H.; Li, X. L.; Kim, J.; Yoo, S.; Deng, T.; Liu, S. J.; Wang, D.; Zheng, W. T. Unifying Miscellaneous Performance Criteria for a Prototype Supercapacitor via Co(OH)$_2$ active Material and Current Collector Interactions. *J. Microsc.* **2017**, *267* (1), 34–48. https://doi.org/10.1111/jmi.12545.

(13)   Oyedotun, K. O.; Masikhwa, T. M.; Mirghni, A. A.; Mutuma, B. K.; Manyala, N. Electrochemical Properties of Asymmetric Supercapacitor Based on Optimized Carbon-Based Nickel-Cobalt-Manganese Ternary Hydroxide and Sulphur-Doped Carbonized Iron-Polyaniline Electrodes. *Electrochim. Acta* **2020**, *334*, 135610. https://doi.org/10.1016/j.electacta.2020.135610.

(14)   Dai, M.; Zhao, D.; Wu, X. Research Progress on Transition Metal Oxide Based Electrode Materials for Asymmetric Hybrid Capacitors. *Chinese Chem. Lett.* **2020**, *31* (9), 2177–2188. https://doi.org/10.1016/j.cclet.2020.02.017.

(15)   Liu, H.; Zhao, D.; Dai, M.; Zhu, X.; Qu, F.; Umar, A.; Wu, X. PEDOT Decorated CoNi2S4 Nanosheets Electrode as Bifunctional Electrocatalyst for Enhanced Electrocatalysis. *Chem. Eng. J.* **2022**, *428*, 131183. https://doi.org/10.1016/j.cej.2021.131183.

(16)   Liu, H.; Zhao, D.; Liu, Y.; Tong, Y.; Wu, X.; Shen, G. NiMoCo Layered Double Hydroxides for Electrocatalyst and Supercapacitor Electrode. *Sci. China Mater.* **2021**, *64* (3), 581–591. https://doi.org/10.1007/s40843-020-1442-3.

(17)   Zhao, D.; Dai, M.; Zhao, Y.; Liu, H.; Liu, Y.; Wu, X. Improving Electrocatalytic Activities of FeCo2O4@FeCo2S4@PPy Electrodes by Surface/Interface Regulation. *Nano Energy* **2020**, *72*, 104715. https://doi.org/10.1016/j.nanoen.2020.104715.

(18)   Luo, M.; Zhao, Z.; Zhang, Y.; Sun, Y.; Xing, Y.; Lv, F.; Yang, Y.; Zhang, X.; Hwang, S.; Qin, Y.; Ma, J. Y.; Lin, F.; Su, D.; Lu, G.; Guo, S. PdMo Bimetallene for Oxygen Reduction Catalysis. *Nature* **2019**, *574*, 81–85. https://doi.org/10.1038/s41586-019-1603-7.

(19)   Ren, B.; Fan, M.; Yang, X.; Wang, L.; Yu, H. 3D Hierarchical Structure Electrodes of MnO2 Nanosheets Decorated on Needle-like NiCo2O4 Nanocones on Ni Foam as a Cathode Material for Asymmetric Supercapacitors. *ChemistrySelect* **2019**, *4* (19), 5641–5650. https://doi.org/10.1002/slct.201901018.

(20)   Xu, K.; Yang, J.; Hu, J. Synthesis of Hollow NiCo2O4 Nanospheres with Large Specific Surface Area for Asymmetric Supercapacitors. *J. Colloid Interface Sci.* **2018**, *511*, 456–462. https://doi.org/10.1016/j.jcis.2017.09.113.

(21)   Chen, W. Q.; Wang, J.; Ma, K. Y.; Li, M.; Guo, S. H.; Liu, F.; Cheng, J. P. Hierarchical NiCo$_2$O$_4$ @Co-Fe LDH Core-Shell Nanowire Arrays for High-Performance Supercapacitor. *Appl. Surf. Sci.* **2018**, *451*, 280–288. https://doi.org/10.1016/j.apsusc.2018.04.254.

(22)   Oyedotun, K. O.; Barzegar, F.; Mirghni, A. A.; Khaleed, A. A.; Masikhwa, T. M.; Manyala, N. Examination of High-Porosity Activated Carbon Obtained from Dehydration

of White Sugar for Electrochemical Capacitor Applications. *ACS Sustain. Chem. Eng.* **2019**, *7* (1), 537–546. https://doi.org/10.1021/acssuschemeng.8b04080.

(23) Zhang, D.; Yan, H.; Lu, Y.; Qiu, K.; Wang, C.; Zhang, Y.; Liu, X.; Luo, J.; Luo, Y. NiCo2O4 Nanostructures Materials: Morphology Control and Electrochemical Energy Storage. J. Chem. Soc. Dalt. Trans. **2014**, 43, 15887-15897. https://doi.org/10.1039/c4dt02276a.

(24) Eskandari, M.; Malekfar, R.; Buceta, D.; Taboada, P. NiCo2O4-Based Nanostructured Composites for High-Performance Pseudocapacitor Electrodes. *Colloids Surfaces A Physicochem. Eng. Asp.* **2020**, *584*, 124039. https://doi.org/10.1016/j.colsurfa.2019.124039.

(25) Li, D.; Gong, Y.; Wang, M.; Pan, C. Preparation of Sandwich-like NiCo2O4/RGO/NiO Heterostructure on Nickel Foam for High-Performance Supercapacitor Electrodes. *Nano-Micro Lett.* **2017**, *9* (2), 1–9. https://doi.org/10.1007/s40820-016-0117-1.

(26) Sudhan, N.; Subramani, K.; Karnan, M.; Ilayaraja, N.; Sathish, M. Biomass-Derived Activated Porous Carbon from Rice Straw for a High-Energy Symmetric Supercapacitor in Aqueous and Nonaqueous Electrolytes. *Energy and Fuels* **2017**, *31* (1), 977–985. https://doi.org/10.1021/acs.energyfuels.6b01829.

(27) Barzegar, F.; Khaleed, A. A.; Ugbo, F. U.; Oyeniran, K. O.; Momodu, D. Y.; Bello, A.; Dangbegnon, J. K.; Manyala, N. Cycling and Floating Performance of Symmetric Supercapacitor Derived from Coconut Shell Biomass. *AIP Adv.* **2016**, *6* (11), 5306. https://doi.org/10.1063/1.4967348.

(28) Gupta, V.; Gupta, S.; Miura, N. Potentiostatically Deposited Nanostructured CoxNi1-x Layered Double Hydroxides as Electrode Materials for Redox-Supercapacitors. *J. Power Sources* **2008**, *175* (1), 680–685. https://doi.org/10.1016/j.jpowsour.2007.09.004.

(29) Xu, L.; Zhang, L.; Cheng, B.; Yu, J. Rationally Designed Hierarchical NiCo2O4– C@Ni(OH)2 Core-Shell Nanofibers for High Performance Supercapacitors. *Carbon N. Y.* **2019**, *152*, 652–660. https://doi.org/10.1016/j.carbon.2019.06.062.

(30) Dai, M.; Zhao, D.; Liu, H.; Zhu, X.; Wu, X.; Wang, B. Nanohybridization of Ni-Co-S Nanosheets with ZnCo2O4Nanowires as Supercapacitor Electrodes with Long Cycling Stabilities. *ACS Appl. Energy Mater.* **2021**, *4* (3), 2637–2643. https://doi.org/10.1021/acsaem.0c03204.

(31) Dai, M.; Liu, H.; Zhao, D.; Zhu, X.; Umar, A.; Algarni, H.; Wu, X. Ni Foam Substrates Modified with a ZnCo2O4Nanowire-Coated Ni(OH)2Nanosheet Electrode for Hybrid Capacitors and Electrocatalysts. *ACS Appl. Nano Mater.* **2021**, *4* (5), 5461–5468. https://doi.org/10.1021/acsanm.1c00825.

(32) Zhao, D.; Dai, M.; Liu, H.; Chen, K.; Zhu, X.; Xue, D.; Wu, X.; Liu, J. Sulfur-Induced Interface Engineering of Hybrid NiCo2O4@NiMo2S4 Structure for Overall Water Splitting and Flexible Hybrid Energy Storage. *Adv. Mater. Interfaces* **2019**, *6* (21), 1–10. https://doi.org/10.1002/admi.201901308.

(33) Wang, J.; Polleux, J.; Lim, J.; Dunn, B. Pseudocapacitive Contributions to Electrochemical Energy Storage in TiO2 (Anatase) Nanoparticles. *J. Phys. Chem. C* **2007**,

111 (40), 14925–14931. https://doi.org/10.1021/jp074464w.

(34)   Pandolfo, A. G. G.; Hollenkamp, A. F. F. Carbon Properties and Their Role in Supercapacitors. *J. Power Sources* **2006**, *157* (1), 11–27. https://doi.org/10.1016/j.jpowsour.2006.02.065.

(35)   Oyedotun, K. O.; Madito, M. J.; Momodu, D. Y.; Mirghni, A. A.; Masikhwa, T. M.; Manyala, N. Synthesis of Ternary NiCo-MnO2nanocomposite and Its Application as a Novel High Energy Supercapattery Device. *Chem. Eng. J.* **2018,** 335, 416-433. https://doi.org/10.1016/j.cej.2017.10.169.

(36)   Sui, Y.; Ye, A.; Qi, J.; Wei, F.; He, Y.; Meng, Q.; Ren, Y.; Sun, Z. Construction of NiCo2O4@Ni0.85Se Core-Shell Nanorod Arrays on Ni Foam as Advanced Materials for an Asymmetric Supercapacitor. *J. Alloys Compd.* **2019**, *778*, 234–238. https://doi.org/10.1016/j.jallcom.2018.10.354.

(37)   Chen, S.; Yang, G.; Jia, Y.; Zheng, H. Three-Dimensional NiCo2O4@NiWO4 Core-Shell Nanowire Arrays for High Performance Supercapacitors. *J. Mater. Chem. A* **2017**, *5* (3), 1028–1034. https://doi.org/10.1039/c6ta08578d.

(38)   Wei, C.; Huang, Y.; Chen, M.; Yan, J.; Yao, W.; Chen, X. Fabrication of Porous Nanosheets Assembled from NiCo2O4/NiO Electrode for Electrochemical Energy Storage Application. *J. Colloid Interface Sci.* **2017**, *504*, 1–11. https://doi.org/10.1016/j.jcis.2017.05.027.